


Article

Tennantite–Tetrahedrite-Series Minerals and Related Pyrite in the Nibao Carlin-Type Gold Deposit, Guizhou, SW China

Dongtian Wei ^{1,2,*}, Yong Xia ^{2,*}, Jeffrey A. Steadman ³, Zhuojun Xie ², Xijun Liu ¹, Qinqing Tan ² 
and Ling'an Bai ¹

¹ Guangxi Key Laboratory of Exploration for Hidden Metallic Ore Deposits, College of Earth Sciences, Guilin University of Technology, Guilin 541006, China; xijunliu@glut.edu.cn (X.L.); bailingan@glut.edu.cn (L.B.)

² State Key Laboratory of Ore Deposit Geochemistry, Institute of Geochemistry, Chinese Academy of Sciences, Guiyang 550002, China; xiezhuojun@vip.gyig.ac.cn (Z.X.); tanqinqing@vip.gyig.ac.cn (Q.T.)

³ Centre for Ore Deposit and Earth Sciences, University of Tasmania, Private Bag 79, Tasmania 7001, Australia; jeff.steadman@utas.edu.au

* Correspondence: weidongtian@glut.edu.cn or weidongtian2016@163.com (D.W.); xiayong@vip.gyig.ac.cn (Y.X.)

Abstract: A number of sediment-hosted, Carlin-type/-like gold deposits are distributed in the Youjiang basin of SW China. The gold ores are characterized by high As, Hg, and Sb contents but with low base metal contents (Cu+Pb+Zn < 500–1000 ppm). The Nibao deposit is unique among these gold deposits by having tennantite–tetrahedrite-series minerals in its ores. The deposit is also unique in being primarily hosted in the relatively unreactive siliceous pyroclastic rocks, unlike classic Carlin-type gold deposits that are hosted in carbonates or calcareous clastic rocks. In this study, we have identified tennantite-(Zn), tennantite-(Hg), and tetrahedrite-(Zn) from the tennantite–tetrahedrite-series mineral assemblage. The tennantite-(Zn) can be further divided into two sub-types of Tn-(Zn)-I; and Tn-(Zn)-II. Tn-(Zn)-I; usually occurs in the core of a Tennantite–tetrahedrite composite and appears the darkest under the SEM image, whereas Tn-(Zn)-II overgrows on Tn-(Zn)-I and is overgrown by tetrahedrite-(Zn). Tennantite-(Hg) occasionally occurs as inclusions near the uneven boundary between Tn-(Zn)-I and Tn-(Zn)-II. An appreciable amount of Au (up to 3540 ppm) resides in the tennantite–tetrahedrite-series minerals, indicating that the latter is a major Au host at Nibao. The coexistence of tennantite–tetrahedrite-series minerals and Au-bearing pyrite indicates the Nibao ore fluids were more oxidized than the Carlin-type ore fluids. The tennantite–tetrahedrite series at Nibao evolved from Tn-(Zn)-I through Tn-(Zn)-II to tetrahedrite-(Zn), which is likely caused by Sb accumulation in the ore fluids. This indicates that the Nibao ore fluids may have become more reduced and less acidic during Au precipitation.

Keywords: tennantite; tetrahedrite; pyrite; Carlin-type gold deposit; Nibao gold deposit; SW China



Citation: Wei, D.; Xia, Y.; Steadman, J.A.; Xie, Z.; Liu, X.; Tan, Q.; Bai, L. Tennantite–Tetrahedrite-Series Minerals and Related Pyrite in the Nibao Carlin-Type Gold Deposit, Guizhou, SW China. *Minerals* **2021**, *11*, 2. <https://dx.doi.org/10.3390/min11010002>

Received: 11 November 2020

Accepted: 18 December 2020

Published: 22 December 2020

Publisher's Note: MDPI stays neutral with regard to jurisdictional claims in published maps and institutional affiliations.



Copyright: © 2020 by the authors. Licensee MDPI, Basel, Switzerland. This article is an open access article distributed under the terms and conditions of the Creative Commons Attribution (CC BY) license (<https://creativecommons.org/licenses/by/4.0/>).

1. Introduction

Over 30 Au deposits (total resource: >800 tonnes) were discovered in the Youjiang basin, SW China, making the region the world's second largest Carlin-type/-like gold deposit cluster (Figure 1; [1–5]). These deposits in SW China have three major types of host rocks: (1) Upper Permian–Middle Triassic carbonates, which host the majority of deposits such as the Shuiyindong [6–12]; (2) Middle Triassic calcareous clastic rocks, which host deposits such as the Lannigou [13–15]; and (3) Upper Permian pyroclastic rocks and Indosinian (Triassic) diabase that are related to the end Permian Emeishan large igneous province (ELIP), which host deposits such as the Nibao and Badu [16–18]. Despite the significant lithological differences between the three types of ore host, all the deposits show Carlin-type gold mineralization features, including: (1) rare visible free gold, and the gold is mainly bound structurally within the (arseno)pyrite lattice as Au⁺ [3,11,15,16]; (2) the Au ores are rich in As, Sb, Hg, and Tl, but are poor in Ag (Ag/Au < 5) and

base metals ($\text{Cu}+\text{Pb}+\text{Zn} < \approx 500\text{--}1000$ ppm) [2,19,20]; (3) ore-forming fluids were of low temperature ($\approx 190\text{--}240$ °C), low salinity ($\approx 2\text{--}3$ wt %, NaCl equiv.), and CO_2 -rich ($\approx 6.3\text{--}8.4$ mol%) [13,21–24]; and (4) ore-related alterations are pervasive and consist of decarbonation, silicic, sulfide, argillic, and dolomite [3,11,16].

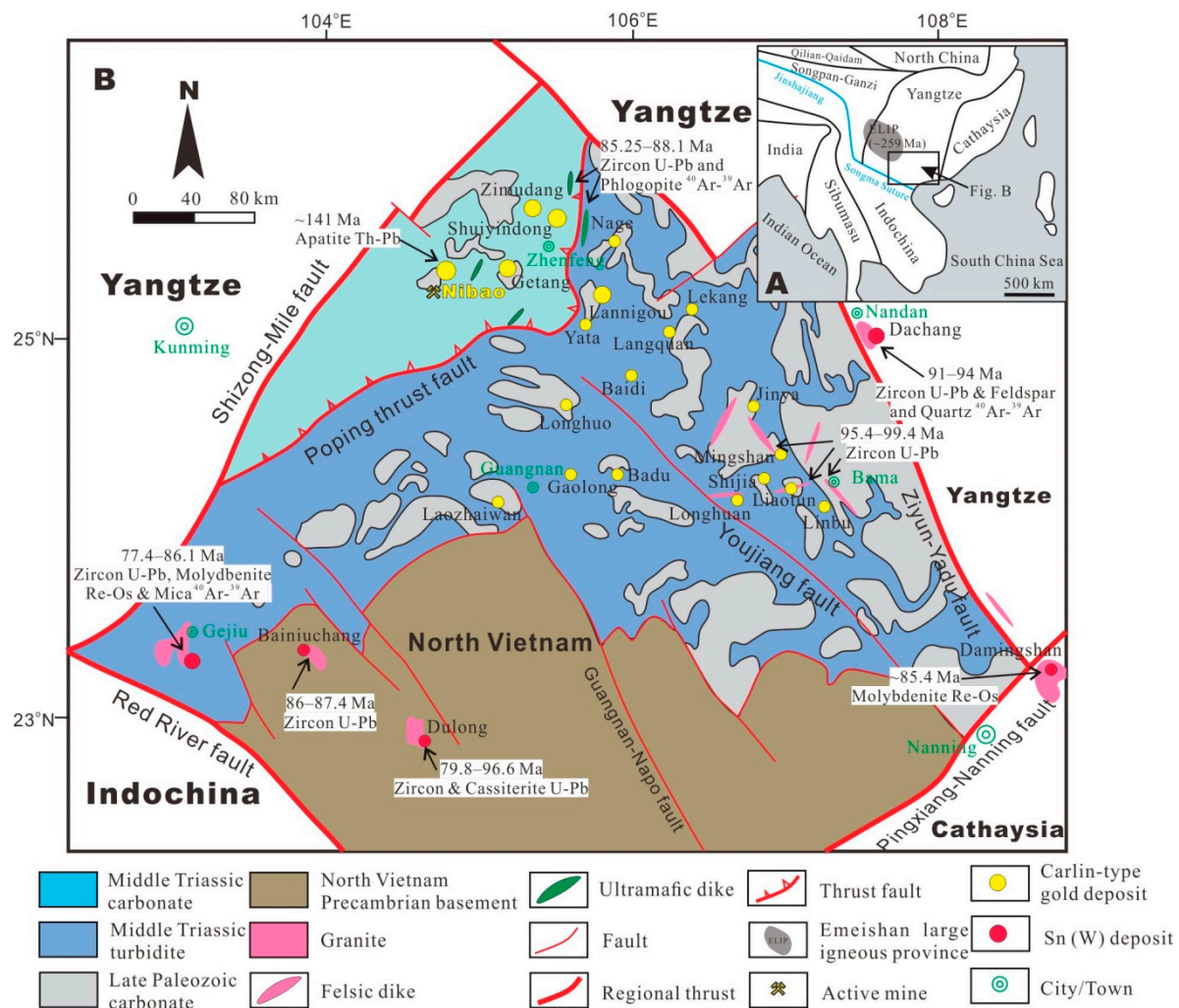


Figure 1. (A) Schematic map showing the tectonic division of SW China–SE Asia around the Youjiang basin; **(B)** Geological map of the Youjiang basin, showing the distribution of the major sedimentary facies, igneous rocks, and gold deposits (modified after Zhu et al., 2017 [25]). Ages of the Sn(W) deposits are summarized from Wang et al. (2004) [26], Li et al. (2008) [27], Cheng and Mao (2010) [28], Cheng et al. (2013) [29], Mao et al. (2013) [30], and Xu et al. (2015) [31]. The ages of the ultramafic and felsic dikes are summarized from Liu et al. (2010) [32] and Zhu et al. (2017) [25], respectively. The age of the Nibao deposit is quoted from Chen et al. (2019) [17].

In the Carlin-type gold deposits of the Youjiang basin, recent in situ analytical studies have demonstrated that the ore-stage pyrite is rich in Cu (≈ 800 ppm; Figure 2; [11,33–35]), and the Cu is suggested to have been leached and transported together with Au in the basin [36]. However, the occurrence of Cu minerals, such as those of the tennantite–tetrahedrite-series, is confined only to a few deposits such as Nibao, and little is known about the chemistry or origin of Cu minerals in these deposits in the Youjiang basin.

The tetrahedrite group minerals contain the tennantite–tetrahedrite solid solution series, which can be expressed as $^{M(2)}\text{A}_6\text{B}^{M(1)}(\text{B}_4\text{C}_2)^{X(3)}\text{D}_4\text{S}^{(1)}\text{Y}_{12}\text{Z}^{S(2)}$, where $\text{A} = \text{Cu}^+$, Ag^+ , \square (vacancy), and $(\text{Ag}_6)^{4+}$ clusters; $\text{B} = \text{Cu}^+$, and Ag^+ ; $\text{C} = \text{Zn}^{2+}$, Fe^{2+} , Hg^{2+} , Cd^{2+} , Mn^{2+} , Cu^{2+} , Cu^+ , and Fe^{3+} ; $\text{D} = \text{Sb}^{3+}$, As^{3+} , Bi^{3+} , and Te^{4+} ; $\text{Y} = \text{S}^{2-}$ and Se^{2-} ; and $\text{Z} = \text{S}^{2-}$, Se^{2-} , and \square [37]. The tennantite series has five minerals, i.e., tennantite-(Fe), tennantite-(Zn),

tennantite-(Cu), tennantite-(Hg) and tennantite-(Mn), whereas the tetrahedrite series has six minerals, i.e., tetrahedrite-(Fe), tetrahedrite-(Zn), tetrahedrite-(Cd), tetrahedrite-(Cu), tetrahedrite-(Hg), and tetrahedrite-(Mn) [37]. Tennantite–tetrahedrite-series minerals are commonly found in various types of mineral systems, including porphyry Cu-Au and related skarn and epithermal deposits, as well as volcanic-hosted massive sulfides (VHMS) and orogenic Au deposits [38–42]. These minerals can structurally incorporate many different trace elements into their crystal lattice and commonly display compositional zoning [39,42]. Such features make tennantite–tetrahedrite-series minerals an important recorder of ore-forming conditions.

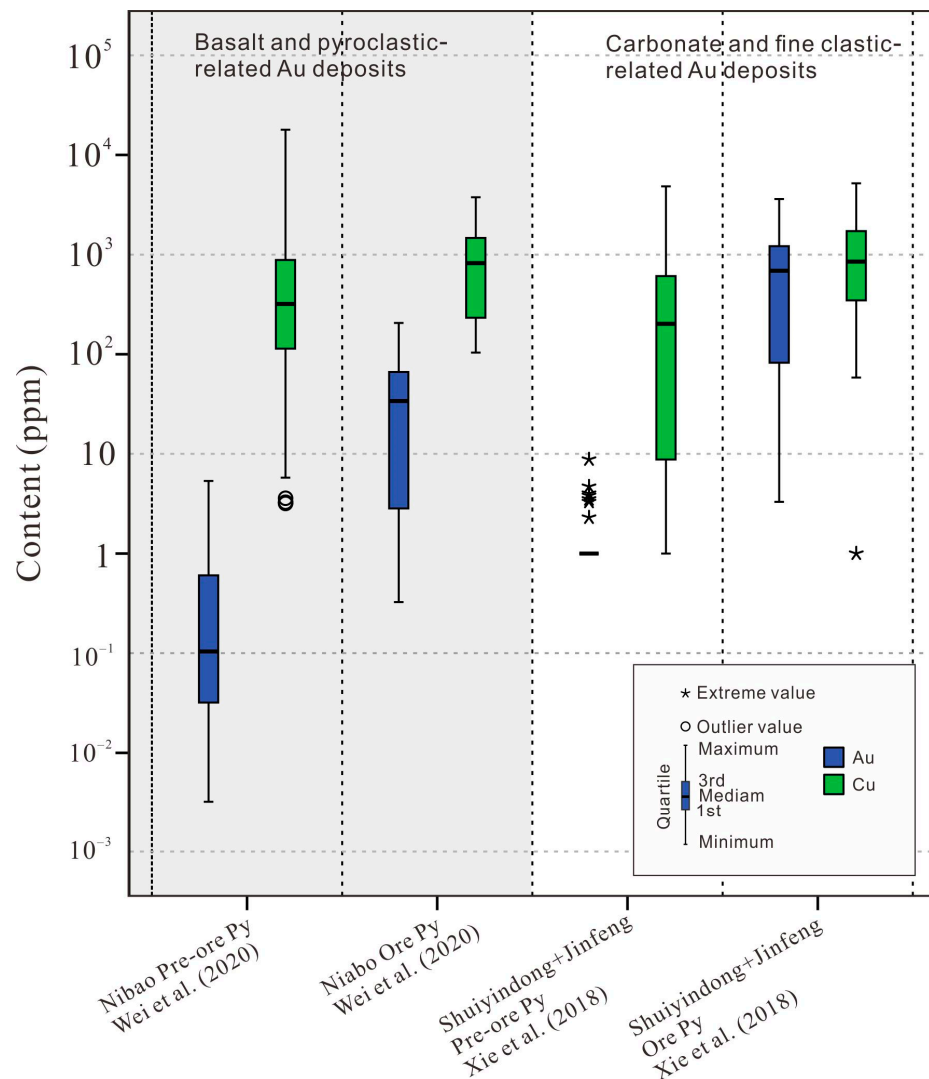


Figure 2. The Au and Cu contents of pre-ore pyrite (Pre-ore Py) and ore pyrite (Ore Py) from the basalt and pyroclastic-related Au deposit and carbonate and fine clastic-related Au deposits (data from Xie et al., 2018 [11] and Wei et al., 2020 [35]).

In this study, we newly reported the geochemical characteristics of tennantite–tetrahedrite–series minerals from Nibao through microanalyses including SEM (Scanning Electron Microscopy) and EPMA (Electron Probe Microanalysis). With these new data, we provide new constraints for the ore-forming conditions at Nibao.

2. Regional Geology

The Youjiang basin is situated on the southwestern (SW) margin of the Yangtze craton (Figure 1A). The basin is bordered by the Mile–Shizong fault in the northwest,

the Ziyun–Yadu fault in the northeast, the Red River fault in the southwest, and the Pingxiang–Nanning fault in the southeast (Figure 1B). The Yangtze craton is interpreted by many authors to have amalgamated with the Cathaysia block to form South China along the Jiangnan orogen at ca. 830 Ma [43,44]. Devonian rifting of the SW margin of the Yangtze craton may have formed the Youjiang basin and produced a series of NW- and NE-striking high-angle basinal faults that controlled the subsequent sedimentation, deformation, and magmatism [3,16,45–47].

The continuous Devonian rifting led to the opening of the Devonian–Carboniferous Ailaoshan–Song Ma Pale–Tethyan ocean branch, and the subsequent extensive deposition of calcareous sandstone, siltstone, shale, and carbonate [47–50]. These rocks host the majority of Carlin-type gold deposits in the Youjiang basin [16]. Following the passive-margin sedimentation, the basin was deformed during the Early Triassic Indochina orogeny, which was caused by the collision between the Indochina and South China blocks [51]. In the late Mesozoic, the Paleo-Pacific subduction beneath South China had likely produced numerous NE-trending folds and faults in the Youjiang basin [52].

Magmatism in the Youjiang basin is dominated by the end Permian ELIP flood basalt, diabase, and pyroclastic rocks. These magmatic rocks host several Carlin-like deposits in the Youjiang basin, such as the Nibao, Jiadi, and Badu. These flood basalt and related pyroclastic rocks (Emeishan Formation) overlie the Dachang Bed (a silicified and brecciated layer) and is overlain by the Upper Permian Longtan Formation [53,54]. Other igneous rocks are scarce in the region, except for some alkaline granites and felsic and ultramafic dikes (ca. 77–99 Ma) ([25–32]; Figure 1B).

3. Deposit Geology

The Nibao gold deposit is situated on the edge of the ELIP flood basalt in the Youjiang basin (Figure 1B), and it hosts a resource (measured plus indicated) of over 60 t Au at ≈ 2.0 g/t [18,35,55]. The Au mineralization age determined by apatite Th–Pb dating is ≈ 141 Ma [17]. Gold mineralization is dominantly fault-controlled and partly stratabound at Nibao ([55,56]; Figure 3).

Local stratigraphic sequence is dominated by carbonate and pyroclastic rocks. The oldest sequence revealed by drilling is the Middle Permian Maokou Formation (Fm.) limestone (> 100 m thick), which is overlain by the silicified and brecciated Dachang Bed (≈ 42 m) [55–57]. Above that lies the Emeishan Formation, which consists of conglomerate, sandstone, siltstone, shale, and coal at the bottom and ELIP basaltic pyroclastic rocks at the top (Figure 4A–E). In turn, this is overlain by the Longtan Fm. (≈ 20 m) interbedded siltstone, mudstone, coal, and limestone. The Emeishan and Longtan Formations are a minor ore host (Orebodies I, II, IV, V and VI). Tennantite–tetrahedrite-series minerals are mainly hosted in the ELIP basaltic pyroclastic rocks of the Emeishan Fm. and siltstone and limestone of Longtan Fm. The Middle Triassic Guanling Formation is distributed in SE Nibao and composed of thick limestone and dolostone (≈ 460 m). Among these sequences, the Emeishan Formation and Dachang Bed are the main ore host ([56–58]; Figure 3B).

Dominant ore-controlling structures at Nibao are the ENE-trending F1 thrust fault, which may have formed by the Indochina orogeny [55], which has developed to be a brecciated alteration zone by later tectono-hydrothermal events (Figures 3B and 4F). Brecciated rocks in F1 thrust fault host the majority of ores (Orebodies III). The F1 thrusting may have also formed the NE-trending Erlongqiangbao anticline. The NS- to NW-striking faults at Nibao may have formed by an NE–SW-directed compressional event [55]. Geologic mapping and drilling have yet to identify any igneous intrusions at Nibao.

At Nibao, ore-related alteration is pervasive and includes a combination of decarbonation, silicic, sulfide, argillic, and dolomite styles [35,57]. Decarbonation (carbonate dissolution) is caused by the calcareous nature of the ore host and the acidic ore-forming fluids ([11,56,57]; Figure 4G). Silicification replaced carbonates in the rocks, and sulfidation involved the sulfide/sulfate precipitation from the H₂S-bearing ore fluids when they reacted

with Fe-bearing wallrocks [21]. Argillization has formed clay minerals such as illite and kaolinite in the ores, whilst dolomitization is manifested by ore-cutting Fe-dolomite veins.

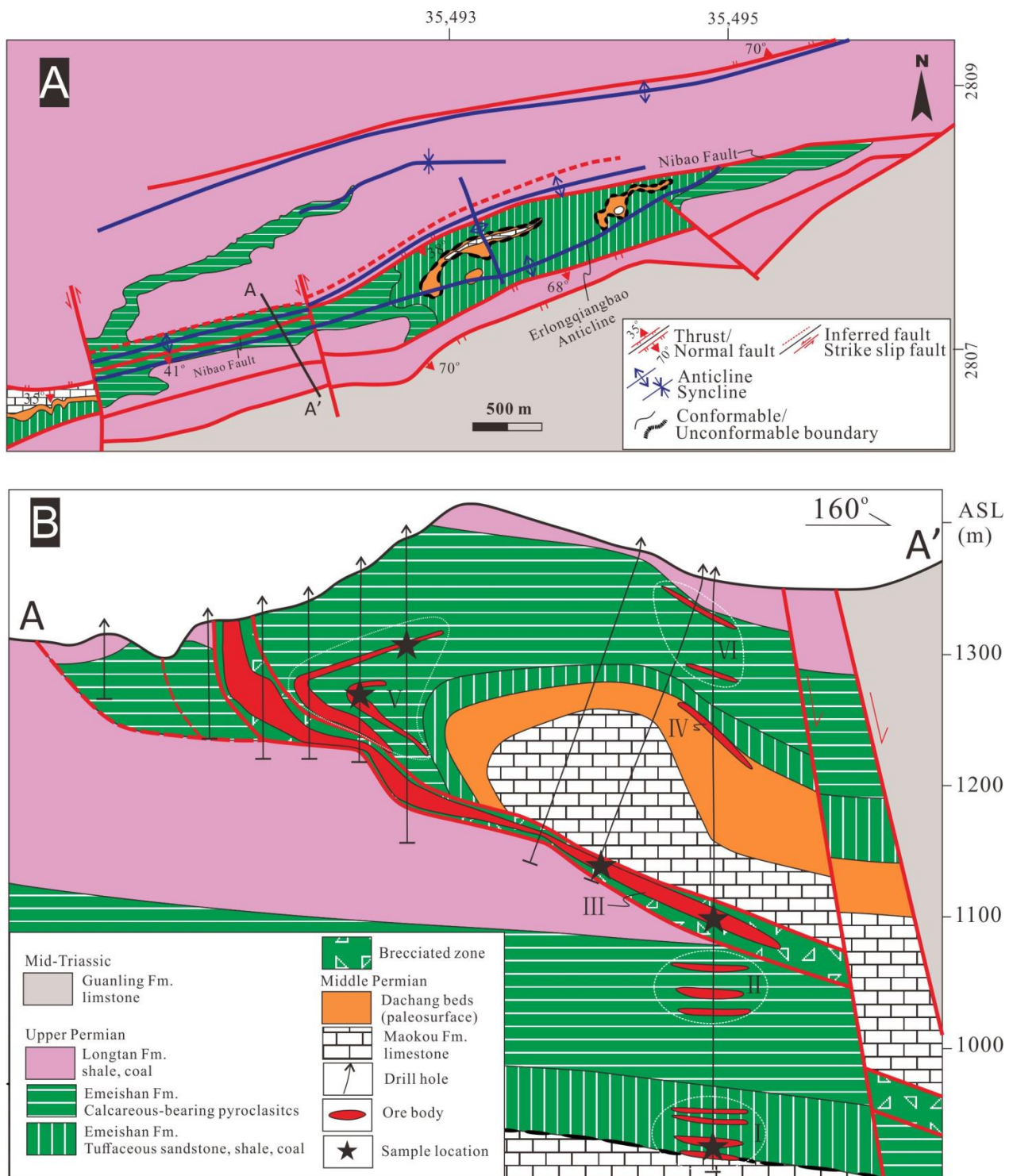


Figure 3. (A) Simplified geologic map of the Nibao gold deposit; (B) A representative geologic cross-section (A–A') at Nibao, showing major structures and stratigraphic units (Qi et al., 2014 [55]; Chen et al., 2019 [17]).

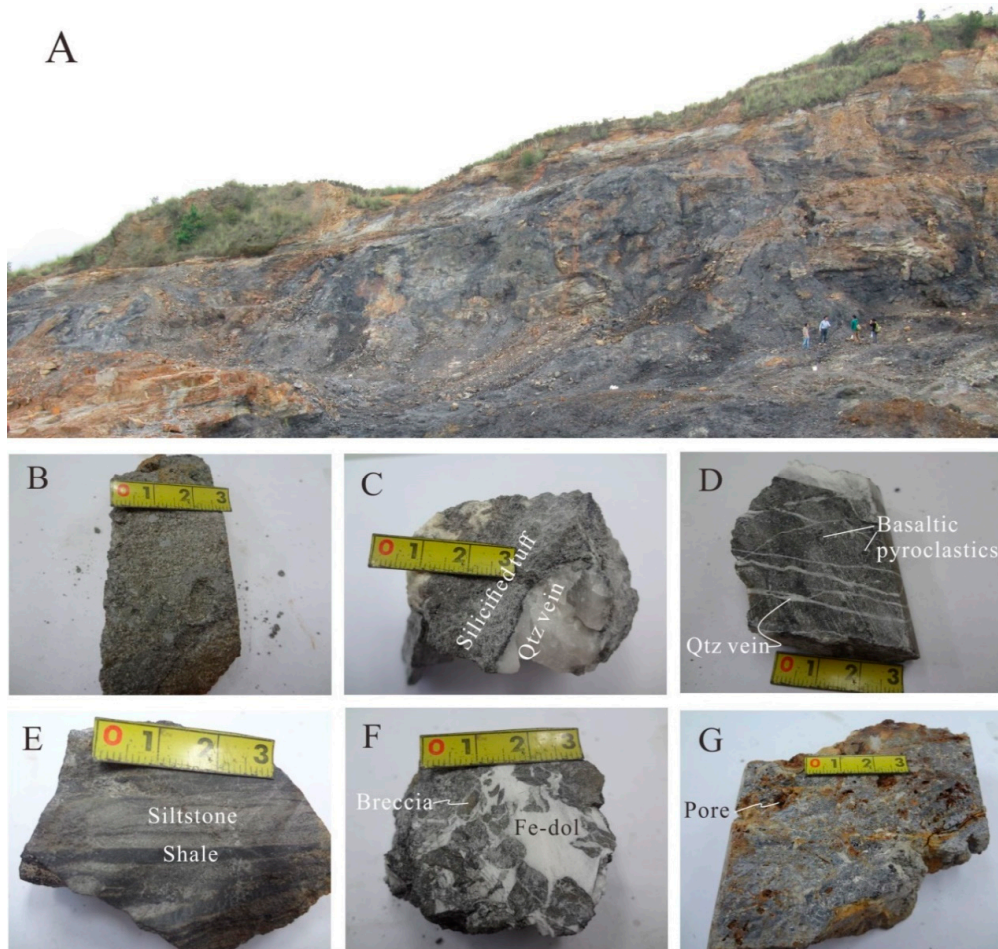


Figure 4. (A) Outcrop photo at Nibao, showing the ore-hosting pyroclastic rocks; (B) Medium-grained ore-hosting tuffaceous conglomerate (lower Emeishan Formation); (C) Silicified ore-hosting tuff (upper Emeishan Formation); (D) Ore-hosting basaltic pyroclastics (upper Emeishan Formation); (E) Ore-hosting tuffaceous siltstone and shale (lower Emeishan Formation); (F) Fe-dolomite-cemented breccia ore (F1 breccia zone); (G) Porous carbonate rocks.

4. Sampling and Analytical Methods

In this study, sixty samples were collected from the Nibao Orebodies I, II, III and V (Figure 3B). The samples were prepared into thin sections to conduct optical microscopic observations and SEM textural and mineralogical analyses. Subsequently, six samples with tennantite–tetrahedrite-series minerals were selected for the EPMA and LA-ICP-MS (Laser Ablation Inductively Coupled Plasma Mass Spectrometry) analyses.

A ΣIGMA Field Emission SEM (Carl Zeiss Microscope Co., Ltd., Oberkochen, Germany) at the Guangxi Key Laboratory of Exploration for Hidden Metallic Ore Deposits (Guilin University of Technology) was used for mineral identification and semi-quantitative mineral geochemical analysis. High-resolution SEM imaging was also conducted to observe textural and mineral paragenetic relations and to provide a guide for positioning the EPMA spots.

The EPMA data were collected with a JXA8230 EPMA (Japan Electron Optics Lab., Tokyo, Japan) at the same laboratory as the SEM analysis. The instrument was operated under the conditions of 15 kV, 20 nA, 2–5 μm-diameter beam size, and measurement of time 10 s (sample) and 5 s (background). The following standards were used: bismuth selenide for Se, arsenopyrite for As, galena for Pb, Greenote (a standard from the Structure Probe, Inc., West Chester, PA, USA) for Cd, manganese oxide for Mn, skutterudite for Co, cuprite for Cu, gold (Au⁰) for Au, silver (Ag⁰) for Ag, stibnite for Sb, pyrite for Fe

and S, sphalerite for Zn, cinnabar for Hg, molybdenite for Mo, and pentlandite for Ni. Minimum detection limits are Se (≤ 100), As (≤ 300 ppm), Pb (≤ 100), Cd (≤ 100), Mn (≤ 100), Co (≤ 100), Cu (≤ 200 ppm), Au (≤ 100 ppm), Ag (≤ 100 ppm), Sb (≤ 110 ppm), S (≤ 1500 ppm), Fe (≤ 600 ppm), Zn (≤ 600 ppm), Hg (≤ 100 ppm), Mo (≤ 100) and Ni (≤ 100 ppm).

LA-ICP-MS pyrite trace element spot analysis and mapping were performed at the Centre for Ore Deposit and Earth Sciences (CODES), University of Tasmania. The instrument consists of a Coherent 193 nm ArF gas-charged excimer laser (Coherent Inc., Wilsonville, OR, USA) and an Agilent 7700 quadrupole ICP-MS (Agilent Tech., Palo Alto, CA, USA). Detailed analytical procedure and operating conditions are as described by Danyushevsky et al. (2011) [59] and Steadman et al. (2015) [60]. The beam sizes chosen (19 to 39 μm) in the spot analyses were dependent on the pyrite size and texture. The spot was pre-ablated with five pulses to eliminate surface contamination. The background was measured for 30 s (laser-off) prior to an 11–60 s measurement of the sample (laser-on). Helium was used as a carrier gas (flux rate: 0.71 L/min). Element mapping was conducted under similar conditions as spot analysis except with a smaller beam diameter (10 or 15 μm) and a 10 Hz pulse rate. A series of parallel lines were ablated at a speed of 10 $\mu\text{m/s}$. Then, the data obtained from parallel ablation lines were used to create trace element images, as described in detail by Steadman et al. (2013) [61].

5. Results

5.1. Textures and EMPA Spot Analyses of Tennantite–Tetrahedrite-Series Minerals

Tennantite–tetrahedrite-series minerals in our samples show a wide range of textures and chemical compositions. Three minerals were recognized, i.e., tennantite-(Zn), tennantite-(Hg), and tetrahedrite-(Zn). Tennantite-(Zn) can be further divided into Tn-(Zn)-I and Tn-(Zn)-II (as described below). A paragenetic assemblage associated with the gold mineralization, involving arsenian pyrite, arsenopyrite, chalcopyrite, sphalerite, tennantite–tetrahedrite-series minerals, realgar–orpiment, quartz, illite, and kaolinite, is present in Figure 5 [17,35,56]). The EMPA spot results, including those of Tn-(Zn)-I (n = 14), Tn-(Zn)-II (n = 124), tennantite-(Hg) (n = 5), and tetrahedrite-(Zn) (n = 35), are summarized in Table 1, with the complete dataset given in Supplementary Table S1.

Minerals	Pre-ore sedimentary–diagenetic stage	Early ore stage	Main ore stage	Late ore stage
As-poor pyrite				
As-rich pyrite				
Arsenopyrite				
Chalcopyrite				
Sphalerite				
Tn-(Zn)-I				
Tn-(Zn)-II				
Tn-(Hg)				
Td-(Zn)				
Realgar-orpiment				
Calcite				
Dolomite				
Quartz				
Illite				
Kaolinite				

Figure 5. Paragenetic sequence of mineralization and alteration at the Nibao Au deposit (after Chen et al., 2018 [56], 2019 [17] and Wei et al. 2020; [35]). Abbreviations: Tn = Tennentite; Td = Tetrahedrite.

Table 1. Summary of EMPA (Electron Probe Microanalysis) data of tennantite–tetrahedrite-series minerals from the Nibao gold deposit.

Element	Tn-(Zn)-I (n = 14)			Tn-(Zn)-II (n = 124)			Tn-(Hg) (n = 5)			Td-(Zn) (n = 35)		
	Min	Max	Avg	Min	Max	Avg	Min	Max	Avg	Min	Max	Avg
wt %												
Pb	-	0.18	0.02	-	0.12	0.01	-	-	-	-	0.10	0.02
Hg	0.17	3.22	1.73	-	3.34	0.95	8.26	16.3	12.7	-	1.39	0.42
Au	-	0.14	0.03	-	0.26	0.04	-	0.09	0.04	-	0.35	0.03
Sb	0.93	1.91	1.28	3.24	14.8	9.68	1.32	3.83	2.22	16.2	26.1	21.4
Ag	-	0.06	0.02	-	0.14	0.05	-	0.02	0.02	-	0.29	0.10
Cd	0.13	0.69	0.34	-	0.70	0.22	1.19	2.72	1.77	-	0.39	0.16
Mo	0.39	0.53	0.46	0.30	0.57	0.42	0.75	1.21	1.05	0.28	0.46	0.37
Se	-	0.13	0.01	-	0.72	0.04	-	0.31	0.06	-	0.51	0.05
As	17.8	19.6	18.7	8.68	17.3	12.9	17.6	18.5	18.0	2.02	8.79	4.91
Zn	5.19	7.11	6.05	5.28	7.56	6.40	1.61	3.51	2.38	5.69	12.5	6.67
Cu	40.2	43.3	41.9	38.2	42.8	40.5	33.2	37.6	34.8	32.3	40.7	39.0
Co	-	0.04	0.01	-	0.05	0.01	-	0.03	0.01	-	0.03	-
Ni	-	0.05	-	-	0.03	-	-	0.03	-	-	0.01	-
Fe	0.93	1.81	1.44	0.52	4.52	1.37	0.53	1.03	0.75	0.35	3.47	1.43
Mn	-	0.04	0.01	-	0.05	0.01	-	0.03	0.01	-	0.04	-
S	26.7	27.6	27.0	24.4	28.0	26.2	26.0	26.4	26.2	23.7	29.0	25.1
apfu												
Pb	-	0.01	-	-	-	-	-	-	-	-	-	-
Hg	0.01	0.24	0.13	-	0.26	0.07	0.65	1.34	1.04	-	0.10	0.03
Au	-	0.01	-	-	0.02	-	-	-	-	-	0.03	-
Sb	0.11	0.23	0.16	0.40	1.92	1.25	0.17	0.50	0.29	2.09	3.58	2.87
Ag	-	-	-	-	0.02	-	-	-	-	-	0.04	0.01
Cd	0.01	0.09	0.04	-	0.09	0.03	0.17	0.40	0.25	-	0.05	0.02
Mo	0.06	0.08	0.07	0.04	0.09	0.06	0.12	0.21	0.18	0.04	0.07	0.06
Se	-	0.02	-	-	0.14	-	-	0.06	0.01	-	0.11	0.01
As	3.65	3.98	3.82	1.82	3.51	2.72	3.81	4.05	3.95	0.45	1.91	1.06
Zn	1.22	1.65	1.41	1.23	1.78	1.53	0.40	0.86	0.59	1.43	2.98	1.66
Cu	9.86	10.2	10.0	9.41	10.4	10.0	8.63	9.46	8.99	7.90	10.3	10.0
Co	-	0.01	-	-	0.01	-	-	-	-	-	-	-
Ni	-	0.01	-	-	-	-	-	0.01	-	-	-	-
Fe	0.25	0.49	0.39	0.14	1.26	0.38	0.15	0.29	0.22	0.10	0.96	0.41
Mn	-	0.01	-	-	0.01	-	-	0.01	-	-	0.01	-
S	12.6	13.0	12.8	12.2	13.6	12.8	13.0	13.5	13.4	12.4	14.0	12.7

Note: “-”: below the detection limit. Atoms per formula unit (apfu) is based on 29 atoms. Abbreviations: Tn = tennantite; Td = tetrahedrite.

Tennantite-(Zn)-I usually occurs in the core of a tennantite–tetrahedrite composite and appears as the darkest domain under SEM image, whereas Tn-(Zn)-II overgrows on Tn-(Zn)-I and is overgrown by tetrahedrite-(Zn) (Figure 6A). In some cases, fine-grained Tn-(Zn)-II ($\approx 10 \mu\text{m}$) rims around As-poor pyrite and intergrows with As-pyrite rim (Figure 6B). Coarse-grained Tn-(Zn)-II ($\approx 100\text{--}500 \mu\text{m}$) is euhedral–subhedral, and it occasionally contains pyrite inclusions with Au contents up to 13.71 ppm (LA-ICP-MS data; Figure 6C). In the decarbonate- and argillic-altered samples, medium-grained Tn-(Zn)-II ($\approx 20\text{--}100 \mu\text{m}$) is subhedral–anhedral and intergrows with pyrite, sphalerite, and anatase (Figure 6D–F). The major and minor elements of Tn-(Zn)-I (Table 1) include As (17.80–19.60 wt %), S (26.7–27.60 wt %), Fe (0.93–1.81 wt %), Sb (0.93–1.91 wt %), Cu (40.20–43.30 wt %), Hg (0.17–3.22 wt %), and Zn (5.19–7.11 wt %). Gold in Tn-(Zn)-I is up to 0.14 wt % (avg. 0.03 wt %). Other trace elements enriched in Tn-(Zn)-I include mainly Cd (0.13–0.69 wt %) and Mo (0.39–0.53 wt %). Compared to Tn-(Zn)-I, Tn-(Zn)-II contains less As (8.68–17.30 wt %), Cd (below detection limit (bdl) to 0.34 wt %), Mo (0.30–0.57 wt %) and Hg (bdl to 3.34 wt %), but more Sb (3.24–14.8 wt %) (Table 1).

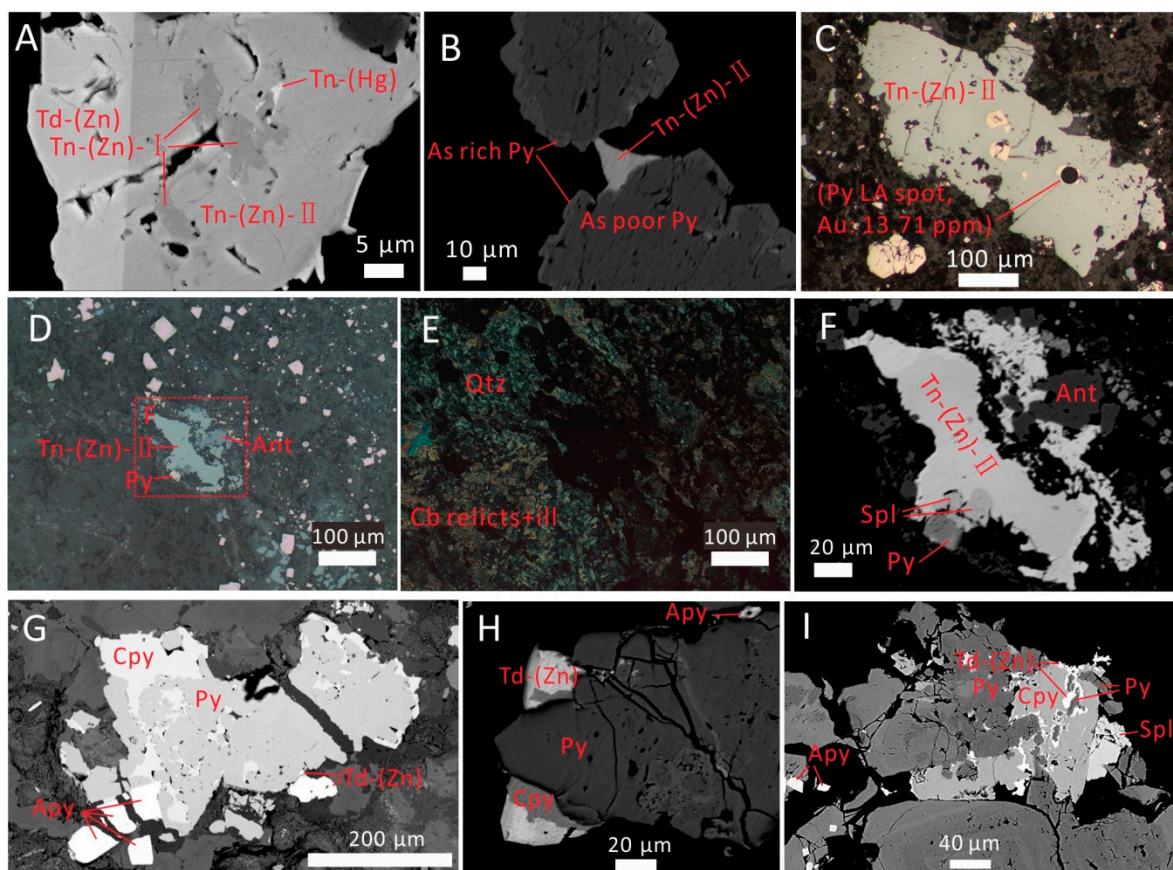


Figure 6. Representative micrographs showing the textures of tennantite–tetrahedrite-series and related mineral assemblage. (A) Tn-(Zn)-I in the core of a tennantite–tetrahedrite composite. Tn-(Zn)-II overgrows on Tn-(Zn)-I, and is overgrown by tetrahedrite-(Zn). Tn-(Hg) inclusions ($\approx 1\text{--}2\ \mu\text{m}$) near the uneven boundary between Tn-(Zn)-I and Tn-(Zn)-II (SEM–BSE); (B) Fine-grained Tn-(Zn)-II ($\approx 10\ \mu\text{m}$) rims around As-poor pyrite and intergrows with As-pyrite rim (SEM–BSE). (C) Coarse-grained ($\approx 100\text{--}500\ \mu\text{m}$) euhedral-subhedral Tn-(Zn)-II with pyrite inclusions (RL); (D–E) Medium-grained ($\approx 20\text{--}100\ \mu\text{m}$) subhedral-anhedral Tn-(Zn)-II intergrows with euhedral pyrite in a decarbonate- and argillic-altered sample (RL and PPL); (F) Close-up view of the Tn-(Zn)-II, pyrite, sphalerite, and anatase assemblage at (D) (SEM–BSE). (G–I) Medium-grained ($\approx 20\text{--}50\ \mu\text{m}$) Td-(Zn) intergrows with pyrite, arsenopyrite, chalcopyrite, and sphalerite (SEM–BSE). Abbreviations: Ant = anatase; Apy = arsenopyrite; Cb = carbonate; Cpy = chalcopyrite; Ill = illite; Td = tetrahedrite; Tn = tennantite; Py = pyrite; Qtz = quartz; Spl = sphalerite; SEM–BSE = Scanning electron microscope with back scattered electrons; RL = reflected light; PPL = plane polarized light.

Tennantite-(Hg) only occurs as inclusions ($\approx 1\text{--}2\ \mu\text{m}$) near the uneven boundary between Tn-(Zn)-I and Tn-(Zn)-II (Figure 6A). Gold content in tennantite-(Hg) is up to 0.09 wt % (avg. 0.04 wt %). Compared with Tn-(Zn), Tn-(Hg) has higher contents of Cd (1.19–2.72 wt %) and Mo (0.75–1.21 wt %), but lower contents of Zn (1.61–3.51 wt %) and Fe (0.53–1.03 wt %) (Table 1).

Tetrahedrite-(Zn) is subhedral-anhedral and fine-medium grained ($\approx 10\text{--}50\ \mu\text{m}$), and commonly intergrows with pyrite, arsenopyrite, chalcopyrite, and sphalerite (Figure 6G–I). Compared with Tn-(Zn) and Tn-(Hg), tetrahedrite-(Zn) has lower Hg content (bdl to 1.39 wt %). Gold content in tetrahedrite-(Zn) is up to 0.35 wt % (avg. 0.03 wt %).

5.2. EMPA (Tennantite–Tetrahedrite–Pyrite) and LA-ICP-MS (Pyrite) Elemental Maps

In the EMPA elemental maps (Figure 7), chemical variations from core to the rim are clear in the tennantite–tetrahedrite–pyrite assemblage. The irregularly-shaped pyrite core (2–4 μm) is rich in S, Co, and Ni, but depleted in As, whereas As is rich outside the core. Compared with the coexisting pyrite, the tennantite–tetrahedrite-series minerals have

relatively high contents of As, Sb, Cu, Zn, and Hg. From the core through inner rim to outer rim of these minerals, the As content decreases while the Sb content increases. Copper, Zn, Hg, and Mo are present throughout the whole tennantite–tetrahedrite.

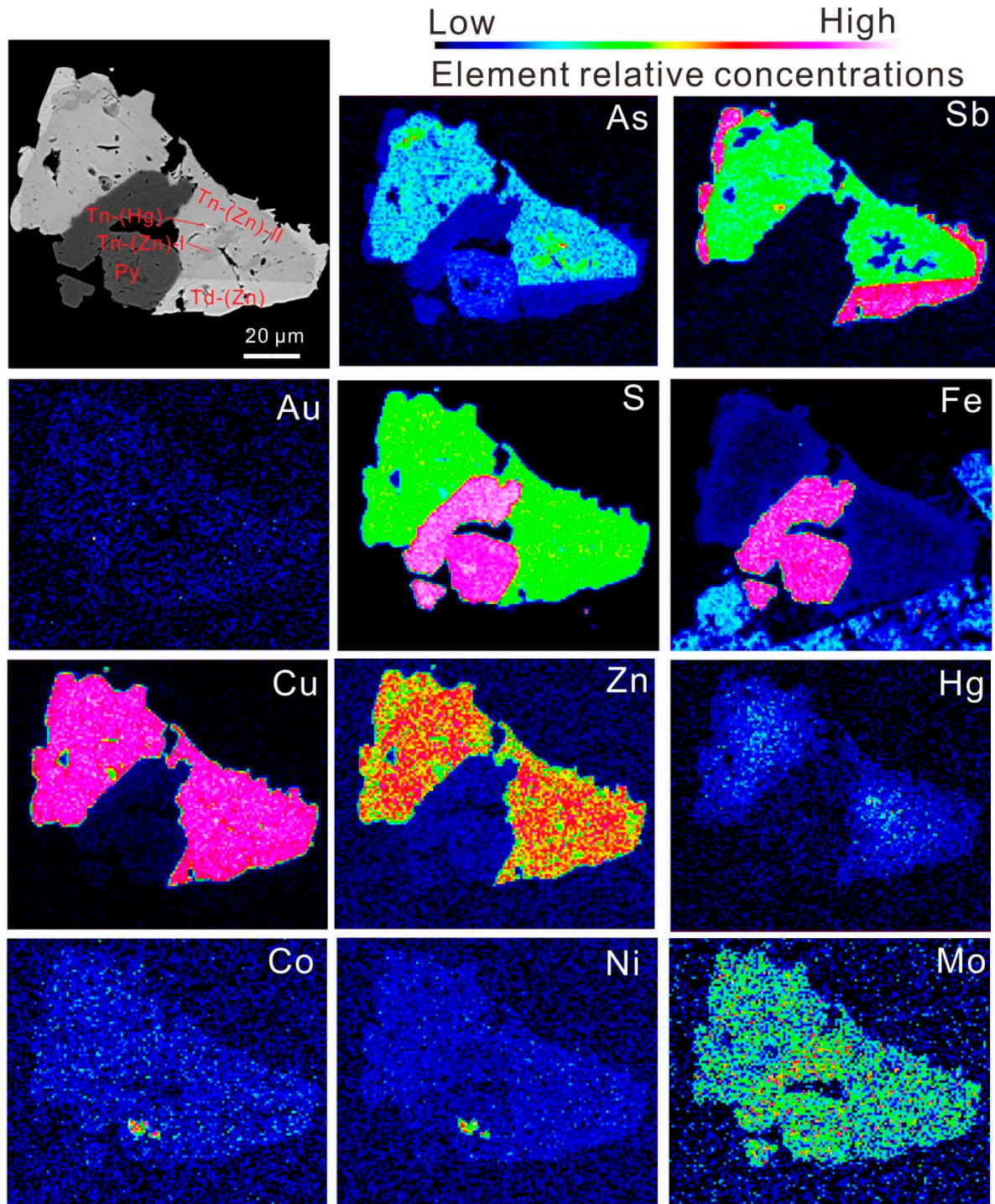


Figure 7. SEM image and EMPA maps of As, Sb, Au, S, Fe, Cu, Zn, Hg, Co, Ni, and Mo in the tennantite–tetrahedrite–pyrite assemblage.

A typical Carlin-type Au-bearing pyrite [20] with an As-poor core and As-rich rim was selected for LA-ICP-MS trace element mapping. The result shows the core has very low Au content, whereas the narrow rim has the highest Au content (Figure 8). Copper (100–500 ppm), As (5000–10,000 ppm), Se (10–100 ppm), Ag (10–50 ppm), Sb (100–1000 ppm), Au (10–100

ppm), Hg (1000–10,000 cps), Tl (10–100 ppm), Pb (10–100 ppm), and Bi (1–5 ppm) are rich in the ore rim, while Co (10–100 ppm) and Ni (10–100 ppm) are concentrated in the porous core. Zinc (1–5 ppm) and Mo (1–5 ppm) are rich in part of the pyrite rim.

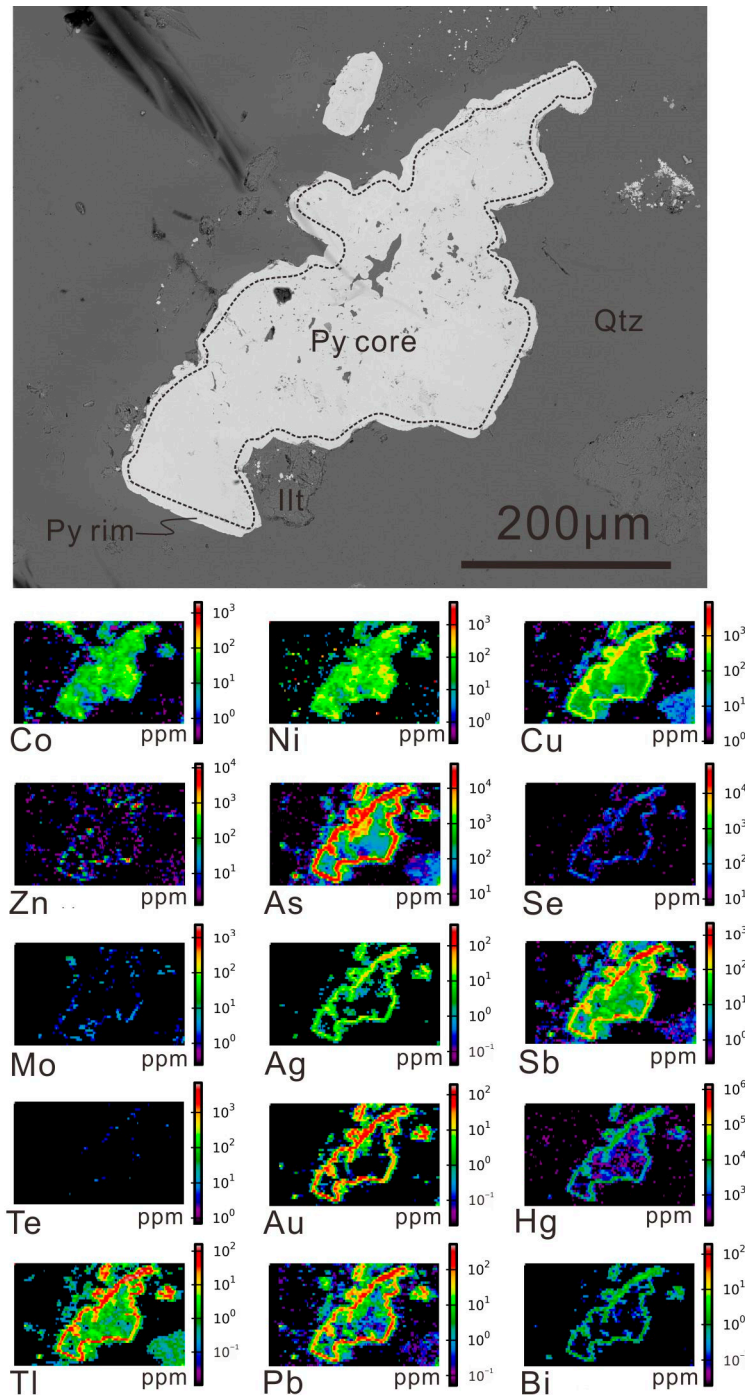


Figure 8. SEM image and LA-ICP-MS maps of Co, Ni, Cu, Zn, As, Se, Mo, Ag, Sb, Te, Au, Hg, Tl, Pb, and Bi in an Au-bearing pyrite grain (with both pre- and syn-ore pyrite). Abbreviations: Illt = illite; Py = pyrite; Pre-ore Py = pre-ore pyrite; Qtz = quartz.

6. Discussion

At Nibao, several lines of evidence support that the tennantite–tetrahedrite-series minerals are ore-related and probably formed during the main-ore to late-ore stage. (1) Samples with tennantite–tetrahedrite-series minerals are from the Au orebodies; (2) Tennantite–

tetrahedrite-series minerals contain varying amounts of Au (Table 1); (3) Coarse-grained tennantite–tetrahedrite-series minerals often contain ore-stage pyrite inclusions (Figure 6C); (4) As observed by Chen et al. (2018) [56], tetrahedrite at Nibao coexists with hydrothermal apatite; (5) Copper precipitation coincided with Au precipitation in the auriferous pyrite grains (Figure 8). Previous studies show that the Cu background concentration in the ELIP basalt is relatively high, e.g., up to 165 ppm Cu in NE Yunnan [62]. The pre-ore sedimentary/diagenetic pyrite Cu contents in the pyroclastic-related Au deposits are higher than those of the carbonate- or fine-clastic sediment-related Au deposits (Figure 2), whereas the syn-ore pyrite Cu contents in these two types of deposits are largely similar. Therefore, it is likely that the Cu in the pyroclastics was leached into the ore fluids and then precipitated in the ore-stage (arseno)pyrite and (mainly) independent Cu minerals, e.g., the tennantite–tetrahedrite-series minerals.

In Carlin-type gold deposits, pyrite and arsenopyrite are the main Au ore minerals, with the gold being structurally bound (Au^+) within the crystal lattice [3,11,15,16]. At Nibao, our result shows that Au not only occurs in pyrite and arsenopyrite but also resides in tennantite–tetrahedrite-series minerals (up to 0.35 wt %, Table 1). In hydrothermal deposits, boiling is usually considered as an important mechanism for Au precipitation, but Au-bearing minerals (pyrite, arsenopyrite, and tennantite–tetrahedrite-series minerals) at Nibao are mostly associated with liquid-rich inclusions [24] rather than aqueous liquid-rich inclusions coexisting with vapor-rich inclusions in the quartz, calcite, and fluorite. At Nibao, the ore host usually contains relicts of ferroan carbonate (Figure 6D,E), indicating that gold-bearing minerals likely precipitated from ore fluids by sulfidation of the ore host, and/or mixing with Fe-rich fluids produced in the alteration zones nearby [16,21,36]. This conclusion is also supported by the lack of As and Au correlation in the tennantite–tetrahedrite-series minerals (Figure 9A). Although it is well known that Au is closely related to As in Carlin-type gold deposits [58,63,64], and pyrite with high As content can host more Au [64], intense fluid–rock interactions may change the ratio of As and Au and affect their partitioning into the tennantite–tetrahedrite-series minerals.

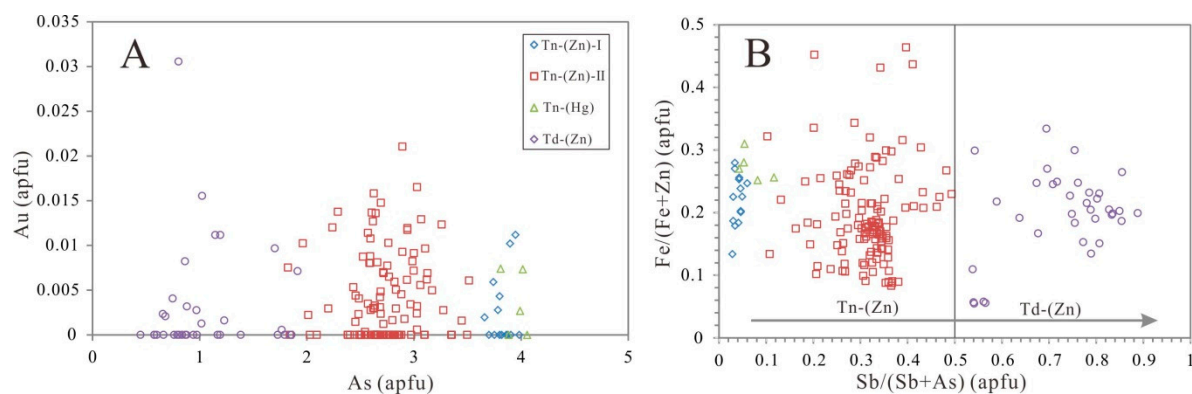


Figure 9. Binary diagrams of As vs. Au (apfu) (A) and Sb/(Sb+As) vs. Fe/(Fe+Zn) (apfu) (B) in tennantite–tetrahedrite-series. Abbreviations: Tn = tennantite; Td = tetrahedrite.

Tennantite–tetrahedrite-series minerals are important ore minerals formed under high oxygen fugacity ($f\text{O}_2$) conditions in porphyry-related mineral systems, including porphyry, skarn, and epithermal polymetallic deposits [37–42,65–67]. Previous studies have shown that the high fluid $f\text{O}_2$ ($\Delta\text{FMQ} > +1.5$ [68–73]) is a key controlling factor for porphyry-related mineralization. High $f\text{O}_2$ can cause sulfide oxidation in magma during the oceanic crust subduction and subsequent post-collision, and it can prevent the early formation of sulfides from supersaturation and precipitation during melt rising and hydrothermal migration [70–73].

Compared with porphyry mineral systems, the $f\text{O}_2$ condition of Carlin-type/-like gold deposits in the Youjiang basin is still poorly constrained due to the lack of suitable mineral

assemblage. Xie et al. (2017) [74] revealed that ore fluids with unusually low fO_2 would enable the uncommon native Sb precipitation at the late-stage Au mineralization, e.g., at the Paiting Carlin-type deposit (carbonate-/fine clastic-hosted) in Guizhou. Unlike Paiting, a main- to late-ore stage mineral at Nibao is tennantite–tetrahedrite series rather than native Sb, indicating that the main- to late-ore fluids at Nibao may have had higher fO_2 than that of the fine clastic-hosted Carlin-type deposits in the region. This conclusion is also supported by the gypsum occurrence in the Nibao orebodies [56]. The higher fO_2 condition may have been attributed to the absence of reductants (e.g., organic matter) in the pyroclastic host rocks at Nibao, cf. the carbonate and fine clastic rocks (organic matter rich) that host the majority of Carlin-type gold deposits in the region.

As shown in Figures 6A and 9B, the core-rim texture of tennantite–tetrahedrite composite indicates that the ore fluids evolved from the Tn-(Zn)-I through Tn-(Zn)-II to tetrahedrite-(Zn) precipitation. During the Tn-(Zn)-I and Tn-(Zn)-II precipitation, arsenopyrite rarely precipitated because As occurs mainly as As^{3+} in Tn-(Zn)-I and Tn-(Zn)-II, indicating that the early-ore fluids are relatively oxidized [66,75]. During the subsequent tetrahedrite-(Zn) precipitation (Figure 9B), As in Tn-(Zn)-I and Tn-(Zn)-II was largely replaced by Sb (average 21.4 wt %, Table 1), indicating that the ore fluids became more reduced [75]. This ore fluid redox conversion may have been a result of intense water–rock interactions and meteoric water incursion, which are both critical mechanism for Au precipitation [7,11,16]. Meanwhile, the pH value may have also modified the compositions of the tennantite-(Zn) and tetrahedrite-(Zn). High pH was reported to favor tetrahedrite formation [75,76], which implies a pH increase during the ore-fluid evolution at Nibao.

7. Conclusions

In this study, tennantite–tetrahedrite-series minerals are recognized to be ore-related in the Nibao deposit, and they probably formed at the main-ore to late-ore stage. The ore-forming fluids at Nibao may have had higher fO_2 than the Carlin-type deposits (carbonate-/fine-clastic-hosted) in the Youjiang basin of SW China. From tennantite-(Zn) to tetrahedrite-(Zn) precipitation, the ore-forming fluids likely evolved to be more reduced and with higher pH.

Supplementary Materials: The following are available online at <https://www.mdpi.com/2075-163X/11/1/2/s1>, Table S1: Complete EMPA spot analysis dataset.

Author Contributions: Y.X. designed the study concept and revised the manuscript; D.W.; J.A.S. contributed to the analysis, data interpretation and manuscript preparation; D.W., Z.X., X.L., Q.T., and L.B. collected the samples; D.W., Z.X., and Q.T. constructed the geologic maps. All authors have read and agreed to the published version of the manuscript.

Funding: This work is supported by the National Key R&D Program of Deep Penetrating Geochemistry (2016YFC0600607), National Natural Science Foundation of China (41963004; 41703046; 41762007; U1812402), Guangxi Science and Technology Base and Talents Special Program (Gui Ke AD19110050), and Science and Technology Foundation of Guizhou Province (Qiankehejichu [2020]1Z034).

Acknowledgments: We are grateful to Team 105 of Guizhou BGMR for sampling access of the Nibao deposit.

Conflicts of Interest: The authors declare no conflict of interest.

References

1. Ashley, R.P.; Cunningham, C.G.; Bostick, N.H.; Dean, W.E.; Chou, I.M. Geology and geochemistry of three sedimentary-rock-hosted disseminated gold deposits in Guizhou Province, People’s Republic of China. *Ore Geol. Rev.* **1991**, *6*, 133–151. [CrossRef]
2. Hu, R.Z.; Su, W.C.; Bi, X.W.; Tu, G.Z.; Hofstra, A.H. Geology and geochemistry of Carlin-type gold deposits in China. *Miner. Depos.* **2002**, *37*, 378–392.
3. Hu, R.Z.; Fu, S.L.; Huang, Y.; Zhou, M.F.; Fu, S.H.; Zhao, C.H.; Wang, Y.J.; Bi, X.W.; Xiao, J.F. The giant South China Mesozoic low-temperature metallogenic domain: Reviews and a new geodynamic model. *J. Asian Earth Sci.* **2017**, *137*, 9–34. [CrossRef]
4. Peters, S.G.; Jiazhan, H.; Zhiping, L.; Chenggui, J. Sedimentary rock-hosted Au deposits of the Dian–Qian–Gui area, Guizhou, and Yunnan Provinces, and Guangxi District, China. *Ore Geol. Rev.* **2007**, *31*, 170–204. [CrossRef]

5. Zhu, J.; Zhang, Z.; Santosh, M.; Jin, Z. Carlin-style gold province linked to the extinct Emeishan plume. *Earth Planet. Sci. Lett.* **2020**, *530*, 115940. [[CrossRef](#)]
6. Liu, J.Z.; Deng, Y.M.; Liu, C.Q.; Xia, Y.; Zhang, X.C.; Tao, Y. Geochemical studies on the inclusion and isotopes of the Shuiyindong gold deposit. *Guizhou Geol.* **2006**, *23*, 51–56, (In Chinese with English abstract).
7. Su, W.C.; Zhang, H.T.; Hu, R.Z.; Ge, X.; Xia, B.; Chen, Y.Y.; Zhu, C. Mineralogy and geochemistry of goldbearing arsenian pyrite from the Shuiyindong Carlin-type gold deposit, Guizhou, China: Implications for gold depositional processes. *Miner. Depos.* **2012**, *47*, 653–662. [[CrossRef](#)]
8. Wang, Z.P.; Xia, Y.; Song, X.Y.; Liu, J.Z.; Yang, C.F.; Yan, B.W. Study on the evolution of ore-formation fluids for Au–Sb ore deposits and the mechanism of Au–Sb paragenesis and differentiation in the southwestern part of Guizhou Province, China. *Chin. J. Geochem.* **2013**, *32*, 56–68. [[CrossRef](#)]
9. Tan, Q.P.; Xia, Y.; Xie, Z.J.; Yan, J. Migration paths and precipitation mechanisms of ore-forming fluids at the Shuiyindong Carlin-type gold deposit, Guizhou, China. *Ore Geol. Rev.* **2015**, *69*, 140–156. [[CrossRef](#)]
10. Tan, Q.P.; Xia, Y.; Wang, X.Q.; Xie, Z.J.; Wei, D.T. Carbon-oxygen isotopes and rare earth elements as an exploration vector for Carlin-type gold deposits: A case study of the Shuiyindong gold deposit, Guizhou Province, SW China. *J. Asian Earth Sci.* **2017**, *148*, 1–12. [[CrossRef](#)]
11. Xie, Z.J.; Xia, Y.; Cline, J.S.; Koenig, A.; Wei, D.T.; Tan, Q.P.; Wang, Z.P. Are There Carlin-Type Gold Deposits in China? A Comparison of the Guizhou, China, Deposits with Nevada, USA, Deposits. In *Diversity of Carlin-Style Gold Deposits, Reviews in Economic Geology*; Muntean, J.L., Ed.; Society of Economic Geologists: Littleton, CO, USA, 2018; Volume 20, pp. 187–233.
12. Tan, Q.; Xia, Y.; Xie, Z.; Wang, Z.; Wei, D.; Zhao, Y.; Yan, J.; Li, S. Two Hydrothermal Events at the Shuiyindong Carlin-Type Gold Deposit in Southwestern China: Insight from Sm–Nd Dating of Fluorite and Calcite. *Minerals* **2019**, *9*, 230. [[CrossRef](#)]
13. Zhang, X.C.; Spiro, B.; Halls, C.; Stanley, C.J.; Yang, K.Y. Sediment-hosted disseminated gold deposits in Southwest Guizhou, PRC: Their geological setting and origin in relation to mineralogical, fluid inclusion, and stable-isotope characteristics. *Int. Geol. Rev.* **2003**, *45*, 407–470. [[CrossRef](#)]
14. Chen, M.H.; Mao, J.W.; Frank, P.B.; Tony, N.; Uttley, P.J. Structural features and metallogensis of the Carlin-type Jinfeng (Lannigou) gold deposit, Guizhou Province, China. *Ore Geol. Rev.* **2011**, *43*, 217–234.
15. Yan, J.; Hu, R.Z.; Liu, S.; Lin, Y.T.; Zhang, J.C.; Fu, S.L. NanoSIMS element mapping and sulfur isotope analysis of Au-bearing pyrite from Lannigou Carlin-type Au deposit in SW China: New insights into the origin and evolution of Au-bearing fluids. *Ore Geol. Rev.* **2018**, *92*, 29–41. [[CrossRef](#)]
16. Su, W.; Dong, W.; Zhang, X.-C.; Shen, N.; Hu, R.; Hofstra, A.; Cheng, L.; Xia, Y.; Yang, K. Carlin-Type Gold Deposits in the Dian-Qian-Gui “Golden Triangle” of Southwest China. In *Diversity of Carlin-Style Gold Deposits, Reviews in Economic Geology*; Muntean, J.L., Ed.; Society of Economic Geologists: Littleton, CO, USA, 2018; Volume 20, pp. 157–185.
17. Chen, M.; Bagas, L.; Liao, X.; Zhang, Z.; Li, Q. Hydrothermal apatite SIMS Th–Pb dating: Constraints on the timing of low-temperature hydrothermal Au deposits in Nibao, SW China. *Lithos* **2019**, *324–325*, 418–428. [[CrossRef](#)]
18. Jin, X.-Y.; Hofstra, A.H.; Hunt, A.G.; Liu, J.-Z.; Yang, W.; Li, J.-W. Noble gases fingerprint the source and evolution of ore-forming fluids of Carlin-type gold deposit in the Golden Triangle, South China. *Econ. Geol.* **2020**, *115*, 455–469. [[CrossRef](#)]
19. Cline, J.S.; Muntean, J.L.; Gu, X.X.; Xia, Y. A Comparison of Carlin-type Gold Deposits: Guizhou Province, Golden Triangle, Southwest China, and Northern Nevada, USA. *Earth Sci. Front.* **2013**, *20*, 1–18.
20. Xie, Z.J.; Xia, Y.; Cline, J.S.; Pribil, M.J.; Koenig, A.; Tan, Q.P.; Wei, D.T.; Wang, Z.P.; Yan, J. Magmatic Origin for Sediment-Hosted Au Deposits, Guizhou Province, China: In Situ Chemistry and Sulfur Isotope Composition of Pyrites, Shuiyindong and Jinfeng Deposits. *Econ. Geol.* **2018**, *113*, 1627–1652. [[CrossRef](#)]
21. Su, W.C.; Heinrich, C.A.; Pettke, T.; Zhang, X.C.; Hu, R.Z.; Xia, B. Sediment-Hosted Gold Deposits in Guizhou, China: Products of Wall-Rock Sulfidation by Deep Crustal Fluids. *Econ. Geol.* **2009**, *104*, 73–93. [[CrossRef](#)]
22. Gu, X.X.; Zhang, Y.M.; Li, B.H.; Dong, S.Y.; Xue, C.J.; Fu, S.H. Hydrocarbon- and ore-bearing basinal fluids: A possible link between gold mineralization and hydrocarbon accumulation in the Youjiang basin, South China. *Miner. Depos.* **2012**, *47*, 663–682. [[CrossRef](#)]
23. Peng, Y.; Gu, X.; Zhang, Y.; Liu, L.; Wu, C.; Chen, S. Ore-forming process of the Huijiabao gold district, southwestern Guizhou Province, China: Evidence from fluid inclusions and stable isotopes. *J. Asian Earth Sci.* **2014**, *93*, 89–101. [[CrossRef](#)]
24. Xie, X.Y.; Feng, D.S.; Chen, M.H.; Guo, S.X.; Kuang, S.D.; Chen, H.S. Fluid inclusion and stable isotope geochemistry study of the Nibao gold deposit, Guizhou and insight into ore genesis. *Acta Petrol. Sin.* **2016**, *32*, 3360–3376, (in Chinese with English abstract).
25. Zhu, J.-J.; Hu, R.-Z.; Richards, J.P.; Bi, X.-W.; Stern, R.; Lu, G. No genetic link between Late Cretaceous felsic dikes and Carlin-type Au deposits in the Youjiang basin, Southwest China. *Ore Geol. Rev.* **2017**, *84*, 328–337. [[CrossRef](#)]
26. Wang, D.H.; Chen, Y.C.; Chen, W.; Sang, H.Q.; Li, H.Q.; Lu, Y.F.; Chen, K.L.; Lin, Z.M. Dating of the Dachang superlarge tin-polymetallic deposit in Guangxi and its implication for the genesis of the No. 100 orebody. *Acta Geol. Sin. (English Ed.)* **2004**, *78*, 452–458.
27. Li, S.; Wang, D.; Liang, T.; Qu, W.; Ying, L. Metallogenic epochs of the Damingshan tungsten deposit in Guangxi and its prospecting potential. *Acta Geol. Sin.* **2008**, *82*, 873–879, (In Chinese with English abstract).
28. Cheng, Y.; Mao, J. Age and geochemistry of granites in Gejiu area, Yunnan province, SW China: Constraints on their petrogenesis and tectonic setting. *Lithos* **2010**, *120*, 258–276.

29. Cheng, Y.; Mao, J.; Spandler, C. Petrogenesis and geodynamic implications of the Gejiu igneous complex in the western Cathaysia block, South China. *Lithos* **2013**, *175–176*, 213–229. [[CrossRef](#)]
30. Mao, J.W.; Cheng, Y.B.; Chen, M.H.; Pirajno, F. Major types and time–space distribution of Mesozoic ore deposits in South China and their geodynamic settings. *Miner. Depos.* **2013**, *48*, 267–294.
31. Xu, B.; Jiang, S.-Y.; Wang, R.; Ma, L.; Zhao, K.-d.; Yan, X. Late Cretaceous granites from the giant Dulong Sn-polymetallic ore district in Yunnan Province, South China: Geochronology, geochemistry, mineral chemistry and Nd–Hf isotopic compositions. *Lithos* **2015**, *218–219*, 54–72. [[CrossRef](#)]
32. Liu, S.; Su, W.; Hu, R.; Feng, C.; Gao, S.; Coulson, I.M.; Wang, T.; Feng, G.; Tao, Y.; Xia, Y. Geochronological and geochemical constraints on the petrogenesis of alkaline ultramafic dykes from southwest Guizhou Province, SW China. *Lithos* **2010**, *114*, 253–264. [[CrossRef](#)]
33. Hou, L.; Peng, H.J.; Ding, J.; Zhang, J.R.; Zhu, S.B.; Wu, S.Y.; Wu, Y.; Ouyang, H.G. Textures and In Situ Chemical and Isotopic Analyses of Pyrite, Huijiabao Trend, Youjiang Basin, China: Implications for Paragenesis and Source of Sulfur. *Econ. Geol.* **2016**, *111*, 331–353. [[CrossRef](#)]
34. Hu, X.; Gong, Y.; Zeng, G.; Zhang, Z.; Wang, J.; Yao, S. Multistage pyrite in the Getang sediment-hosted disseminated gold deposit, southwestern Guizhou Province, China: Insights from textures and in situ chemical and sulfur isotopic analyses. *Ore Geol. Rev.* **2018**, *99*, 1–16. [[CrossRef](#)]
35. Wei, D.-T.; Xia, Y.; Gregory, D.D.; Steadman, J.A.; Tan, Q.-P.; Xie, Z.-J.; Liu, X.-j. Multistage pyrites in the Nibao disseminated gold deposit, southwestern Guizhou Province, China: Insights into the origin of Au from textures, in situ trace elements, and sulfur isotope analyses. *Ore Geol. Rev.* **2020**, *122*, 103446. [[CrossRef](#)]
36. Chen, J.; Huang, Z.-L.; Yang, R.-D.; Du, L.-J.; Liao, M.-Y. Gold and antimony metallogenic relations and ore-forming process of Qinglong Sb(Au) deposit in Youjiang basin, SW China: Sulfide trace elements and sulfur isotopes. *Geosci. Front.* **2020**. [[CrossRef](#)]
37. Biagioni, C.; George, L.L.; Cook, N.J.; Makovicky, E.; Moelo, Y.; Pasero, M.; Sejkora, J.; Stanley, C.J.; Mark, D.W.H.; Bosi, F. The tetrahedrite group: Nomenclature and classification. *Am. Mineral.* **2020**, *105*, 109–122. [[CrossRef](#)]
38. Vavelidis, M.; Melfos, V. Bi-Ag-bearing tetrahedrite-tennantite in the Kapsalina copper mineralisation, Thasos island, Northern Greece. *Neues Jb. Miner. Abh.* **2004**, *180*, 149–169. [[CrossRef](#)]
39. Sack, R.O.; Lichtner, P.C. Constraining Compositions of Hydrothermal Fluids in Equilibrium with Polymetallic Ore-Forming Sulfide Assemblages. *Econ. Geol.* **2009**, *104*, 1249–1264. [[CrossRef](#)]
40. Catchpole, H.; Kouzmanov, K.; Fontbote, L. Copper-Excess Stannoidite and Tennantite-Tetrahedrite as Proxies for Hydrothermal Fluid Evolution in a Zoned Cordilleran Base Metal District, Morococha, Central Peru. *Can. Mineral.* **2012**, *50*, 719–743. [[CrossRef](#)]
41. George, L.L.; Cook, N.J.; Ciobanu, C.L. Minor and Trace Elements in Natural Tetrahedrite-Tennantite: Effects on Element Partitioning among Base Metal Sulphides. *Minerals* **2017**, *7*, 17. [[CrossRef](#)]
42. Marushchenko, L.L.; Baksheev, I.A.; Nagornaya, E.V.; Chitalin, A.F.; Nikolaev, Y.N.; Vlasov, E.A. Compositional evolution of the tetrahedrite solid solution in porphyry-epithermal system: A case study of the Baimka Cu-Mo-Au trend, Chukchi Peninsula, Russia. *Ore Geol. Rev.* **2018**, *103*, 21–37. [[CrossRef](#)]
43. Zhao, J.-H.; Zhou, M.-F.; Yan, D.-P.; Zheng, J.P.; Li, J.W. Reappraisal of the ages of Neoproterozoic strata in South China: No connection with the Grenvillian orogeny. *Geology* **2011**, *39*, 299–302. [[CrossRef](#)]
44. Yao, J.; Shu, L.; Cawood, P.A.; Li, J. Delineating and characterizing the boundary of the Cathaysia Block and the Jiangnan orogenic belt in South China. *Precambrian Res.* **2016**, *275*, 265–277. [[CrossRef](#)]
45. Zeng, Y.; Liu, W.; Chen, H.; Zheng, R.; Zhang, J.; Li, X.; Jiang, T. Evolution of Sedimentation and Tectonics of the Youjiang Composite Basin, South China. *Acta Geol. Sin.* **1995**, *69*, 113–124, (in Chinese with English abstract).
46. Du, Y.S.; Huang, H.; Yang, J.H.; Huang, H.W.; Tao, P.; Huang, Z.Q.; Hu, L.S.; Xie, C.X. The basin translation from Late Paleozoic to Triassic of the Youjiang basin and its tectonic signification. *Geol. Rev.* **2013**, *59*, 1–11, (In Chinese with English abstract).
47. Lai, C.-K.; Meffre, S.; Crawford, A.J.; Zaw, K.; Xue, C.-D.; Halpin, J.A. The Western Ailaoshan Volcanic Belts and their SE Asia connection: A new tectonic model for the Eastern Indochina Block. *Gondwana Res.* **2014**, *26*, 52–74. [[CrossRef](#)]
48. Lai, C.K.; Meffre, S.; Crawford, A.J.; Zaw, K.; Halpin, J.A.; Xue, C.D.; Salam, A. The Central Ailaoshan ophiolite and modern analogs. *Gondwana Res.* **2014**, *26*, 75–88. [[CrossRef](#)]
49. Xia, X.; Nie, X.; Lai, C.-K.; Wang, Y.; Long, X.; Meffre, S. Where was the Ailaoshan Ocean and when did it open: A perspective based on detrital zircon U–Pb age and Hf isotope evidence. *Gondwana Res.* **2016**, *36*, 488–502. [[CrossRef](#)]
50. Yang, J.; Cawood, P.A.; Du, Y.; Huang, H.; Hu, L. Detrital record of Indosinian mountain building in SW China: Provenance of the Middle Triassic turbidites in the Youjiang Basin. *Tectonophysics* **2012**, *574–575*, 105–117. [[CrossRef](#)]
51. Metcalfe, I. Tectonic framework and Phanerozoic evolution of Sundaland. *Gondwana Res.* **2011**, *19*, 3–21. [[CrossRef](#)]
52. Dai, C.; Wang, M.; Chen, J.; Wang, X. Tectonic movement characteristic and its geological significance of Guizhou. *Guizhou Geol.* **2013**, *30*, 119–124, (In Chinese with English abstract).
53. Liu, J.Z.; Chen, J.H.; Deng, Y.M.; Fu, Z.K.; Chen, F.E.; Chen, M.; You, B. Exploration of the Shuiyindong super-scale gold deposit and the evolution of exploration for metallogenic belt of the Huijiabao anticline in Guizhou Province. *Geol. Survey Res.* **2009**, *32*, 138–143, (In Chinese with English abstract).
54. Sun, J.; Nie, G.; Huang, S.; Fu, B.; Chen, S. A research of ore-forming conditions of Nibao gold deposit in Guizhou Province, China. *J. Guizhou Univ. (Nat. Sci. Ed.)* **2012**, *29*, 36–41, (In Chinese with English abstract).

55. Qi, L.S.; He, Y.N.; Qi, J.; Yang, T.C.; Zhang, M.M.; Zheng, Y.; Zhang, C. New cognizance of orebody type and formation mechanism of Nibao gold deposit in Guizhou. *Guizhou Geol.* **2014**, *31*, 109–115, (In Chinese with English abstract).
56. Chen, M.H.; Guo, S.X.; Xie, X.Y.; Ma, K.Z. Hydrothermal mineralogy of Nibao Carlin-type gold deposit, Guizhou Province and its geological significances. *Miner. Depos.* **2018**, *37*, 502–520, (In Chinese with English abstract).
57. Chen, M.H.; Xie, X.Y.; Ma, K.Z. Research on lithology and stratigraphy conditions of fault-controlled orebody in Nibao Carlin-type gold deposit, Guizhou Province. *Gold Sci. Technol.* **2018**, *26*, 131–142, (In Chinese with English abstract).
58. Zheng, L.; Yang, R.; Gao, J.; Chen, J.; Liu, J.; He, Y. Geochemical characteristics of the giant Nibao Carlin-type gold deposit (Guizhou, China) and their geological implications. *Arab. J. Geosci.* **2016**, *9*, 108. [[CrossRef](#)]
59. Danyushevsky, L.; Robinson, P.; Gilbert, S.; Norman, M.; Large, R.; McGoldrick, P.; Shelley, M. Routine quantitative multi-element analysis of sulphide minerals by laser ablation ICP-MS: Standard development and consideration of matrix effects. *Geochem. Explor. Environ. A.* **2011**, *11*, 51–60. [[CrossRef](#)]
60. Steadman, J.A.; Large, R.R.; Meffre, S.; Olin, P.H.; Danyushevsky, L.V.; Gregory, D.D.; Belousov, I.; Lounejeva, E.; Ireland, T.R.; Holden, P. Synsedimentary to early diagenetic gold in black shale-hosted pyrite nodules at the Golden Mile Deposit, Kalgoorlie, western Australia. *Econ. Geol.* **2015**, *110*, 1157–1191. [[CrossRef](#)]
61. Steadman, J.A.; Large, R.R.; Meffre, S.; Bull, S.W. Age, origin and significance of nodular sulfides in 2680Ma carbonaceous black shale of the Eastern Goldfields Superterrane, Yilgarn Craton, Western Australia. *Precambrian Res.* **2013**, *230*, 227–247. [[CrossRef](#)]
62. Li, Z.; Ye, L.; Huang, Z.; Zhou, J.; Hu, Y.; Nian, H. Mineralogical characteristics and geological significance of copper minerals in Fule Pb-Zn deposit, Yunnan Province, China. *Geol. J. China Univ.* **2018**, *24*, 200–209, (In Chinese with English abstract).
63. Reich, M.; Kesler, S.E.; Utsunomiya, S.; Palenik, C.S.; Chryssoulis, S.L.; Ewing, R.C. Solubility of gold in arsenian pyrite. *Geochim. Cosmochim. Acta* **2005**, *69*, 2781–2796. [[CrossRef](#)]
64. Xing, Y.; Brugger, J.; Tomkins, A.; Shvarov, Y. Arsenic evolution as a tool for understanding formation of pyritic gold ores. *Geology* **2019**, *47*, 335–338. [[CrossRef](#)]
65. Petersen, U. Regional geology and major ore deposits of central Peru. *Econ. Geol.* **1965**, *60*, 407–476. [[CrossRef](#)]
66. Wu, I.; Petersen, U. Geochemistry of tetrahedrite and mineral zoning at Casapalca, Peru. *Econ. Geol.* **1977**, *72*, 993–1016. [[CrossRef](#)]
67. Lyubimtseva, N.G.; Bortnikov, N.S.; Borisovsky, S.E. Coexisting Bournonite-Seligmannite and Tennantite-Tetrahedrite Solid Solutions of the Darasun Gold Deposit, Eastern Transbaikalia, Russia: Estimation of the Mineral Formation Temperature. *Geol. Ore Depos.* **2019**, *61*, 274–291. [[CrossRef](#)]
68. Ballard, J.R.; Palin, M.J.; Campbell, I.H. Relative oxidation states of magmas inferred from Ce(IV)/Ce(III) in zircon: Application to porphyry copper deposits of northern Chile. *Contrib. Mineral. Petr.* **2002**, *144*, 347–364. [[CrossRef](#)]
69. Mungall, J.E. Roasting the mantle: Slab melting and the genesis of major Au and Au-rich Cu deposits. *Geology* **2002**, *30*, 915–918. [[CrossRef](#)]
70. Liang, H.-Y.; Sun, W.; Su, W.-C.; Zartman, R.E. Copper-gold mineralization at Yulong, China, promoted by decreasing redox potential during magnetite alteration. *Econ. Geol.* **2009**, *104*, 587–596. [[CrossRef](#)]
71. Sun, W.D.; Liang, H.Y.; Ling, M.X.; Zhan, M.Z.; Ding, X.; Zhang, H.; Yang, X.Y.; Li, Y.L.; Ireland, T.R.; Wei, Q.R.; et al. The link between reduced porphyry copper deposits and oxidized magmas. *Geochim. Cosmochim. Ac.* **2013**, *103*, 263–275. [[CrossRef](#)]
72. Sun, W.; Huang, R.F.; Li, H.; Hu, Y.B.; Zhang, C.C.; Sun, S.J.; Zhang, L.P.; Ding, X.; Li, C.Y.; Zartman, R.E.; et al. Porphyry deposits and oxidized magmas. *Ore Geol. Rev.* **2015**, *65*, 97–131. [[CrossRef](#)]
73. Zhang, H.; Ling, M.-X.; Liu, Y.-L.; Tu, X.-L.; Wang, F.-Y.; Li, C.-Y.; Liang, H.-Y.; Yang, X.-Y.; Arndt, N.T.; Sun, W.-D. High Oxygen Fugacity and Slab Melting Linked to Cu Mineralization: Evidence from Dexing Porphyry Copper Deposits, Southeastern China. *J. Geol.* **2013**, *121*, 289–305. [[CrossRef](#)]
74. Xie, Z.-J.; Xia, Y.; Cline, J.S.; Yan, B.-W.; Wang, Z.-P.; Tan, Q.-P.; Wei, D.-T. Comparison of the native antimony-bearing Paiting gold deposit, Guizhou Province, China, with Carlin-type gold deposits, Nevada, USA. *Miner. Depos.* **2017**, *52*, 69–84. [[CrossRef](#)]
75. Yan, W.; Ouyang, Z.; Li, C. Mineral chemistry of tetrahedrites from Lanping-Simao vein copper deposits, Yunnan Province. *Acta Mineral. Sin.* **1994**, *14*, 361–368, (In Chinese with English abstract).
76. Fu, W.; Yan, W.; Li, F.; Fan, W. A preliminary experimental study on the dissolution of natural tetrahedrite. *Acta Mineral. Sin.* **1994**, *14*, 279–284, (In Chinese with English abstract).